Single-Shot Visualization of Evolving Laser Wakefields Using an All-Optical Streak Camera

Zhengyan Li, Hai-En Tsai, Xi Zhang, Chih-Hao Pai, Yen-Yu Chang, Rafal Zgadzaj, Xiaoming Wang, V. Khudik, G. Shvets, and M. C. Downer

Phys. Rev. Lett. **113**, 085001 — Published 22 August 2014

DOI: 10.1103/PhysRevLett.113.085001

Single-shot visualization of evolving laser wakefields using an all-optical streak camera

Zhengyan Li, Hai-En Tsai, Xi Zhang, Chih-Hao Pai, Yen-Yu Chang, Rafal Zgadzaj, Xiaoming Wang, V. Khudik, G. Shvets, and M. C. Downer
Department of Physics, University of Texas at Austin, Austin, Texas 78712-1081, USA

We visualize ps-time-scale evolution of an electron density bubble — a wake structure created in atmospheric density plasma by an intense ultrashort laser pulse — from the phase "streak" that the bubble imprints onto a probe pulse that crosses its path obliquely. Phase streaks, recovered in one shot using frequency-domain interferometric techniques, reveal formation, propagation and coalescence of the bubble within a 3 mm long ionized helium gas target. 3D particle-in-cell (PIC) simulations validate the observed density-dependent bubble evolution, and correlate it with generation of a quasi-monoenergetic $\sim$ 100 MeV electron beam. The results provide a basis for understanding optimized electron acceleration at plasma density $n_e \approx 2 \times 10^{19}$ cm^{-3}, inefficient acceleration at lower density and dephasing limits at higher density.

The idea of accelerating charged particles by surfing them on laser-driven plasma waves [1] has, after decades of research [2], led to tabletop sources of quasi-monoenergetic [3] GeV electron bunches [4] and ultrafast x-ray pulses [5] for applications in biology, materials science and medicine. Laser-plasma accelerators (LPAs) achieve unprecedented accelerating fields ($\sim$GV/cm), the key to their compact size, by replacing conventional stationary metal structures of the scale of a radio-frequency wavelength ($\sim$ 1 m) with light-speed electron-density structures of the scale of a plasma wavelength $\lambda_p \sim 10^{-4}$ m.

The small size and luminal velocity of LPAs, however, makes observation and control of their evolving structure — the main determinant of LPA performance [6, 7] — exceptionally challenging. Consequently, LPA science has relied on intensive computer simulations with estimated initial conditions for visualizing the dynamic microstructure of laser-driven plasma waves. Nevertheless direct laboratory visualization is essential when initial conditions are imprecisely known. This is particularly true for the highest-performing LPAs, which operate in a strongly nonlinear "bubble" regime that favors efficient injection of surrounding plasma electrons [6] and quasi-monoenergetic acceleration [7]. In this regime, the LPA can be sensitive to shot-to-shot variations in laser-plasma conditions. Matlis *et al.* used frequency-domain holography (FDH) to record snapshots of laser wakes in a quasi-linear regime in which they evolved negligibly [8]. FDH snapshots in the more nonlinear bubble regime [9], however, averaged over key bubble dynamics that underlie LPA physics [6]. *Dynamic* nonlinear wakes have been visualized only by probing them transversely at different delays over *multiple* shots [10]. However, this method is impractical for LPA experiments with shot-to-shot variations, or low repetition rate.

In this Letter, we report single-shot diagnosis of evolving laser-driven plasma bubbles using an optical frequency-domain streak camera (FDSC) [11], in which a temporally stretched probe pulse crosses the bubble's path at a small oblique angle. In our LPA, optimized electron beams with $\sim$ 100 MeV peak energy, $\sim$ 100 pC charge, $\sim$ 4 mrad divergence are generated reproducibly within a narrow range $\bar{n}_e \sim 2.0 \pm 0.1 \times 10^{19}$ cm^{-3} of plasma density [12], but degrade rapidly in quality at lower and higher density. To understand the underlying physics, FDSC phase streaks that reveal bubble formation, propagation, and coalescence in each shot are compared with particle-in-cell (PIC) simulations. The results show that the location and depth of bubble formation, and the distance the bubble propagates before coalescing with trailing wave structures, depend sensitively on $\bar{n}_e$, and in turn dictate electron energy and beam quality.

To generate plasma wakes, 800 nm, 30 fs, 0.8 J laser pulses polarized along the x-axis (Fig. 1a) were focused ($f/12$) to spot radius 10 μm and normalized vector potential $a_0 = eA/m_e c^2 \approx 1.5$ at the entrance of a supersonic helium gas jet of thickness $L = 3$ mm. A transverse interferometer determined the plasma density profile $\bar{n}_e(r, z)$ on each shot, and a magnetic spectrometer with field $\vec{B}$ along the y-axis (Fig. 1a) analyzed electron energy downstream from the gas jet.

To record phase streaks, a reference-probe pulse pair (center wavelength $\lambda_{pr} = 400$ nm, bandwidth $\Delta\lambda_{pr} \sim 10$ nm, beam radius $\sim$ 1 mm) split from the drive pulse, then frequency-doubled with $\sim$ 1 mJ energy and polarization orthogonal to the drive pulse to discriminate probe light from scattered, frequency-broadened pump light [13], was chirped (2.7×10^3 fs^2) to duration $\sim$ 500 fs, and propagated at lab angle θ across the pump laser path through the gas jet (Fig. 1a). The reference preceded by $\sim$ 2 ps, and the probe overlapped, the pump and its immediate wake. Thus the plasma column and wake propagating at $v_{pu} = 0.99c$ imprinted a phase shift onto the probe (velocity $v_{pr} \approx c$) as they drifted across its profile at projection angle ϕ to the pump propagation direction (Fig. 1b). Here by choosing $\theta = 8.6°$, we achieved $\phi \approx 90°$ [14] — *i.e.* plasma structures drifted across the probe orthogonally to their propagation direction. The streak thus became a time sequence of transverse projections of the evolving *longitudinal* profiles of the plasma structures, the optimum geometry for observing bubble dynamics behind the pump. To record the phase streak, probe and reference were imaged from the gas jet exit to a spectrometer entrance slit, which selected a $y_{pr} = y_0$ slice of their profiles. Interference of the reference with the phase-modulated probe in the spectrometer yielded a frequency-domain hologram (Fig. 1a), which a charge-

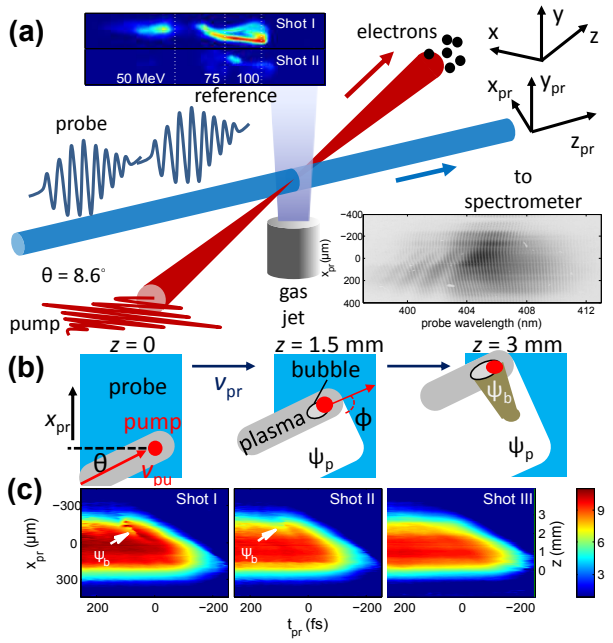

FIG. 1. **(a)** Schematic FDSC setup. Pump (x,y,z) and probe $(x_{\rm pr},y_{\rm pr},z_{\rm pr})$ coordinates share a common $y = y_{\rm pr}$ axis. Upper left: electron spectra for two shots at $\bar{n}_e = 1.7 \times 10^{19}$ cm^{-3}, illustrating shot-to-shot variations. Lower right: typical frequency-domain interferogram. **(b)** Lateral drift of plasma structures across probe profile (blue rectangle), viewed from $+y$ axis. **(c)** Reconstructed probe phase shift $\psi(t_{\rm pr}, x_{\rm pr})$ for three shots at $\bar{n}_e = 1.7 \times 10^{19}$ cm^{-3}, illustrating variations of bubble phase dip $\psi_{\rm b}$. The $t_{\rm pr}$ axis corresponds to probe wavelength axis in (a). Right vertical axis: propagation distance z corresponding to $x_{\rm pr}$. Color bar: phase shift in rad.

coupled device (CCD) recorded. Fourier transformation of the hologram [8] reconstructed the probe phase shift map $\psi(t_{\rm pr}, x_{\rm pr})$ (Fig. 1c), where $t_{\rm pr}$ denotes time delay in the probe co-moving frame, $x_{\rm pr}$ transverse position in the probe profile. Since max (ψ) usually exceeded 2π, a 2D phase unwrapping procedure [15] was applied.

As shown in Fig. 1b, both the quasi-static plasma column of width $d_{\rm p} \sim 200$ μm behind the ionization front, and the dynamic bubble of width $d_{\rm b} \approx \lambda_p\sqrt{a_0}/\pi \sim 10$ to 20μm [16], blown out by the drive pulse after relativistically self-focusing to high a_0, contributed to ψ. The former contributed $\psi_{\rm p} \simeq (2\pi/\lambda_{\rm pr})(\bar{n}_e/4n_{\rm c})(d_{\rm p}/\sin\theta)$, where $n_{\rm c} = 7.0\times10^{21}$ cm^{-3} is the critical density for a 400 nm probe. Thus for $\bar{n}_e \sim 1.7 \times 10^{19}$ cm^{-3}, $\psi_{\rm p} \sim 12$ rad, consistent with measured max $(\psi) \approx 10$ rad (Fig. 1c). The latter contributed $\psi_{\rm b} \sim 1$ to 2 rad, opposite in sign to $\psi_{\rm p}$, due to the absence of free electrons in the bubble. Thus after a bubble forms, $\psi_{\rm b}$ carved a narrow dip into the broader $\psi_{\rm p}$ profile. Shot-to-shot fluctuations in the $\psi_{\rm b}(x_{\rm pr}, t_{\rm pr})$ profiles and electron spectra were observed at all $\bar{n}_e$, but became pronounced near the threshold for self-injection of plasma electrons into the plasma bubble (*i.e.* $\bar{n}_e \sim 1.7 \times 10^{19}$ cm^{-3}), as illustrated by Fig. 1a (upper left inset) and c. When no bubble formed and no relativistic electrons were observed, no phase dip was observed, as shown in Fig. 1c, right panel.

Fig. 2 shows evolution of the bubble "dip" at 4 different $\bar{n}_e$ for propagation distances $1 < z < 3$ mm, as revealed by line-outs of the phase streaks at regular intervals perpendicular to their axes. The bubble dips appeared immediately behind the pump, whose drift trajectory is shown by dashed lines. For all cases, no dip was observed for $z < 1$ mm, where the pump pulse was still self-focusing before blowing out a bubble. For $z > 1$ mm, evolution of the dip depended strongly on $\bar{n}_e$. For $\bar{n}_e = 1.3 \times 10^{19}$ cm^{-3} (Fig. 2a), hardly any phase shift dip was observed, indicating no "bubble" formed. This is consistent with a null signal on the electron spectrometer (Fig. 2a, top). Accelerated electrons first appeared near $\bar{n}_e = 1.7 \times 10^{19}$ cm^{-3} (Fig. 2b, top), albeit inconsistently (Fig. 1a, upper left inset). Here the ratio $P/P_{\rm cr}$ of laser power to the critical power for relativistic self-focusing was ~ 6, within the range of Froula's empirical threshold for self-injection [17]. FDSC corroborated this threshold by revealing the correlated appearance of a bubble phase shift dip (Fig. 2b, main panel). First evident at $z \approx 2$ mm, the dip formed fully at $z = 2.5$ mm, leaving ~ 0.5 mm acceleration length, less than the dephasing length $L_{\rm d} \simeq (2\lambda_{\rm p}^3\sqrt{a_0})/(3\pi\lambda^2) \approx 0.6$ mm [16]. Acceleration was thus incomplete, consistent with low electron energy (< 80 MeV), broad spectrum and high rms pointing instability (~ 20 mrad) observed at this $\bar{n}_e$. Moreover, FDSC revealed that the bubble was incompletely evacuated at injection threshold, evident from the shallowness ($\psi_{\rm b} \sim 1$ rad) of the fully-formed phase dip, compared to higher $\bar{n}_e$. At optimal plasma density $\bar{n}_e \sim 2.0 \times 10^{19}$ cm^{-3} (Fig. 2c), the dip appeared at $z = 1.5$ mm, then formed fully ($\psi_b \sim 2$ mrad, ~ 50 fs width) at $z = 2.0$ mm. This bubble accelerated electrons quasi-monoenergetically to 100 MeV (Fig. 2c, top) with low shot-to-shot fluctuations and high pointing stability. Here $L_{\rm d} \sim 0.5$ mm, so electrons injected into the bubble at $z \sim 2.0$ mm would accelerate to the dephasing point near $z \sim 2.5$ mm. For $z > 2.5$ mm, the phase dip shifted backward from the pump and widened. At $\bar{n}_e \sim 2.2\times10^{19}$ cm^{-3} (Fig. 2d), the phase dip formed fully (2 rad depth) at $z \approx 1.5$ mm due to faster self-focusing. But with $L_{\rm d} \sim 0.3$ mm, injected electrons accelerated only to $z \sim 1.8$ mm, after which the phase dip again shifted backwards from the pump and widened. These dynamics yielded lower energy electrons with a broad spectrum and poor beam quality (Fig. 2d, top).

To help understand the results in Fig. 2, we used the 3D particle-in-cell code Virtual Laser Plasma Lab (VLPL) [18] to simulate a 30 fs Gaussian pump pulse with $a_0 = 1.2$ and $w_0 = 10$ μm propagating into 3-mm plasma with $1 < \bar{n}_e < 2 \times 10^{19}$ cm^{-3}. The simulations revealed trends that closely mirrored those in Fig. 2, except that a given bubble dynamic and electron spectrum occurred at 20 to 30% lower $\bar{n}_e$ than in the experiments. This discrepancy is due to the higher quality, and more effective self-focusing, of the simulated drive pulse, and highlights the need for laboratory visualization to supplement simulations and for simulations with non-ideal

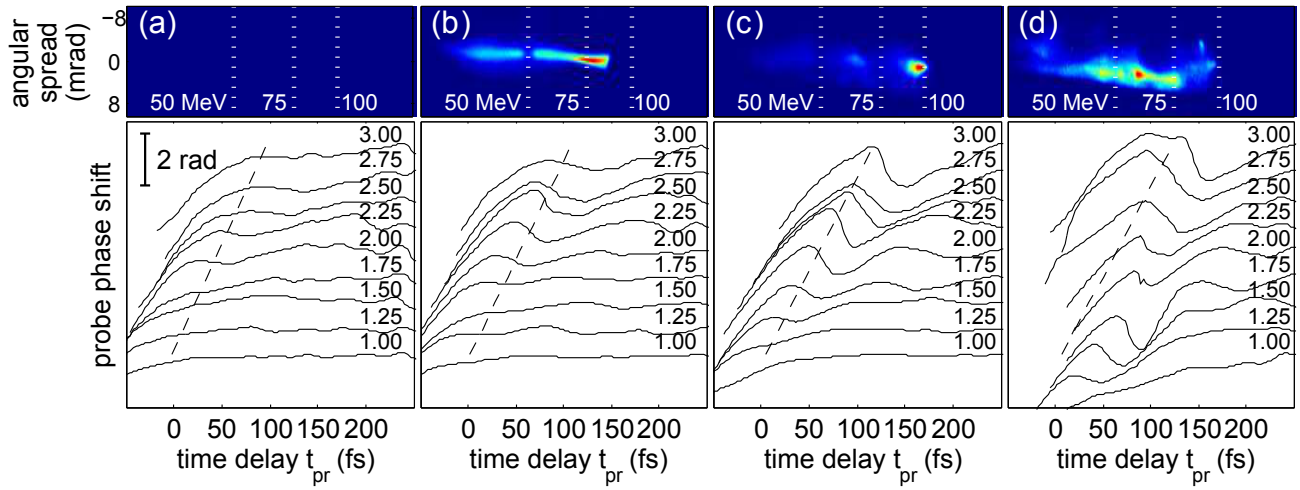

FIG. 2. Electron spectra and probe phase streak line-outs at densities **(a)** 1.3; **(b)** 1.7; **(c)** 2.0; **(d)** 2.2×10^{19} cm^{-3}. Numbers on each curve denote propagation distance z in millimeters. Dashed lines show trajectory of center of pump pulse.

beams [19].

Fig. 3 shows representative simulation results. Optimum acceleration was observed at $\bar{n}_e = 1.5 \times 10^{19}$ cm^{-3}. As in experiments at 2.0×10^{19} cm^{-3} (Fig. 2c), the simulated pump formed a bubble at $z \approx 1.6$ mm (Fig. 3a) after self-focusing. Electrons self-injected into a deepening, lengthening bubble [6] near $z = 2.0$ mm (Fig. 3b), and accelerated to $z \approx 2.4$ mm, where the primary bubble merged with the trailing one due to beam loading, forming a long blow-out channel (Fig. 3c). These bubble dynamics closely mirror the phase dip dynamics in Fig. 2c. Moreover, the simulation yielded quasi-monoenergetic 100 MeV electrons (Fig. 3d), in agreement with experiment (Fig. 2c, top) and with the prediction of

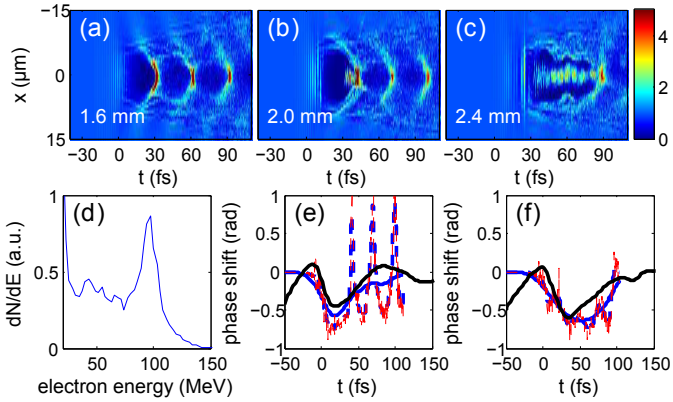

FIG. 3. VLPL simulations for $\bar{n}_e = 1.5 \times 10^{19}$ cm^{-3}. **(a-c)** Density profiles at $z = 1.6$ **(a)**, 2.0 **(b)** and 2.4 mm **(c)**, representing initial bubble formation, full blowout/injection, and coalescence, respectively. **(d)** Calculated electron spectrum. **(e-f)** Bubble phase shift perturbation ψ_b on top of $\psi_p \sim 13$ rad at $z = 2.0$ **(e)** and $z = 2.6$ mm **(f)** for ideal unlimited-bandwidth probe (red), and probes of 100 (blue dashed) and 10 nm (blue solid) bandwidth, compared with measured ψ_b for $\bar{n}_e = 2 \times 10^{19}$ cm^{-3} (black solid). Measured ψ_b was divided by ~ 2 to correct for higher $\bar{n}_e$ in the experiment.

Lu's phenomenological model [16]. Moreover, the simulation revealed the function of the short dephasing region ($z > 2.5$ mm) observed by FDSC: it decelerated faster electrons just enough that slower electrons caught up, compressing the spectrum [20].

To relate simulated plasma density profiles $n_e(t, x, y, z)$ to FDSC results, we calculated the phase shift $\psi(t, z) = (2\pi/\lambda_{\rm pr} \sin\theta) \int \eta(t, x, y_0, z) \mathrm{d}x$ that the plasma refractive index profile $\eta(t, x, y, z) = \sqrt{1 - n_e(t, x, y, z)/\gamma(t, x, y, z) n_c}$ induced on the probe for selected z. Here t denotes time behind the center of the pump, and the integration over x describes drift of the index object across the probe profile. Red curves in Fig. 3e,f and Fig. 4 show calculated phase shift line-outs $\psi(t_{\rm pr}, z)$ for an ideal probe with unlimited bandwidth. In practice, finite probe bandwidth limits temporal resolution to $\delta t \approx 30$ fs, and was taken into account by convolving $\psi(t, z)$ with a Gaussian function with FWHM $\delta t = 30$ fs, yielding the blue solid curves. These are compared with measured phase shifts (black solid curves) in Fig. 3e and f.

The results in Fig. 3e,f demonstrate that FDSC with $\Delta\lambda_{\rm pr} = 30$ nm fully resolves the longitudinal $\Delta n_e/n_e$ profile of the main bubble cavity, and detects bubble lengthening that accompanies beam loading. The absolute value of $\Delta n_e/n_e$ is calibrated by independently measuring the width and density of the surrounding plasma by transverse interferometry. Although these dynamics were widely predicted by simulations, here they are observed for the first time in the laboratory, enabling unprecedented correlation with electron beam properties and simulations. The FDSC results also reveal two aspects of bubble physics that were *not* widely anticipated by simulations. First, they show that at injection threshold (Fig. 2b), the bubble is only partially evacuated. Second, they show that moderate dephasing contributes beneficially to optimizing the electron beam (Fig. 2c) by compressing its spectrum. FDSC can potentially access additional physics by resolving the sub-micron electron-

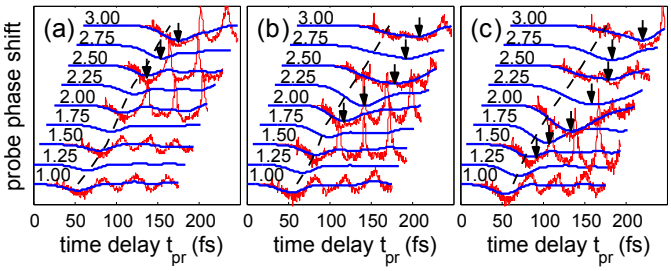

FIG. 4. Calculated probe phase shift due to VLPL-simulated wake profiles for ideal probe (red) and 10 nm bandwidth probe (blue) at $\bar{n}_e = 1.2$ **(a)**, 1.5 **(c)**, and 1.7×10^{19} cm^{-3} **(d)**. Dashed lines are pump trajectories. Arrows highlight bubble phase dip minima in blue curves, which correspond to measured dynamics in Fig. 2b-d.

density sheath that anisotropically surrounds the bubble through the use of supercontinuum probe/reference pulses. For example, a 100 nm-bandwidth probe could resolve the sheath sufficiently well (blue dashed curve, Fig. 3e,f) to quantitatively study subtle thickness variations related to injection physics [20]. However, in contrast to previous supercontinuum interferometry [21], a mJ-energy UV ($\lambda_{\rm pr} < 450$ nm) continuum source will need to be developed to obtain high signal/noise-ratio interferograms in the presence of strong background pump-driven supercontinuum [13]. Additional probes at $\theta < 8.6°$ can potentially visualize radial dynamics, enabling tomographic reconstruction of the complete bubble profile [14]. However, background light strengthens at smaller θ [13], and radial bubble dynamics play no substantial role under the current conditions. Thus the FDSC configuration in Fig. 1a accesses the most essential physics with the fewest technical complications.

Fig. 4 presents calculated phase shifts for three $\bar{n}_e$ that correspond to Fig. 2b-d. At $\bar{n}_e = 1.0 \times 10^{19}$ cm^{-3} (not shown), only a barely perceptible phase dip occurs, since no bubble was excited. Near injection threshold (Fig. 4a), a clear bubble phase dip appeared (highlighted by arrows), reaching full depth ($\psi_b \sim 1$ rad) at $z \approx 2.5$ mm. At optimal density (Fig. 4b), the bubble phase dip formed fully at $z \sim 2.0$ mm, then widened for $z > 2.5$ mm. In the over-acceleration regime (Fig. 4c), a fully developed bubble phase dip emerged at $z = 1.5$ mm, then widened for $z > 2$ mm. These calculated trends closely mirror those exhibited in the data in Fig. 2b-d.

In conclusion, we measured dynamics of a laser-driven plasma bubble accelerator in a single shot using a frequency-domain streak camera [11]. FDSC data identified the major stages of bubble evolution — formation, stable propagation, broadening and coalescence — over a 10 ps interval with < 0.5 ps resolution. 3D PIC simulations reproduced FDSC and acceleration results, and correlated them with underlying physics: relativistic self-focusing, electron injection into a fully formed bubble, dephasing, and bubble coalescence due to beam loading.

This work was supported by DOE grants DE-SC0011617 and DE-SC0007889 and by the NSF-DOE Partnership in Plasma Science program. Z. L. acknowledges support of a Glenn Focht Memorial Fellowship in Laser Physics.

[1] T. Tajima and J. M. Dawson, Phys. Rev. Lett. **43**, 267–270 (1979).
[2] E. Esarey, C. B. Schroeder, W. P. Leemans, Rev. Mod. Phys. **81**, 1229–1285 (2009).
[3] S. P. D. Mangles et al., Nature **431**, 535–538 (2004); C. G. R. Geddes, et al., Nature **431**, 538–541 (2004); J. Faure, et al., Nature **431**, 541–544 (2004).
[4] W. P. Leemans *et al.*, Nature Phys. **2**, 696–699 (2006); N. A. M. Hafz *et al.*, Nature Photon. **2**, 571 (2008); S. Kneip *et al.*, Phys. Rev. Lett. **103**, 035002 (2009); C. E. Clayton *et al.*, Phys. Rev. Lett., **105**, 105003 (2010); X. Wang *et al.*, Nature Commun. **4**, 1988 (2013); H. T. Kim *et al.*, Phys. Rev. Lett. **111**, 165002 (2013).
[5] S. Corde *et al.*, Rev. Mod. Phys. **85**, 1-48 (2013).
[6] S. Y. Kalmykov *et al.*, Phys. Rev. Lett. **103** 135004 (2009).
[7] A. Pukhov, J. Meyer-ter-Vehn, Appl. Phys. B **74**, 355-361 (2002).
[8] N. H. Matlis *et al.*, Nature Phy. **2**, 749–753 (2006).
[9] P. Dong *et al.*, Phys. Rev. Lett. **104**, 134801 (2010).
[10] A. Buck *et al.*, Nature Phys. **7**, 543–548 (2011).
[11] Z. Li *et al.*, Opt. Lett. **35**, 4087–4089 (2010).
[12] H. -E. Tsai *et al.*, AIP Conf. Proc. **1507**, 330–335 (2012).
[13] J. E. Ralph *et al.*, Phys. Rev. Lett. **102**, 175003 (2009).
[14] Z. Li *et al.*, Nature Commun. **5**, 3085 (2014).
[15] D. C. Ghiglia and L. A. Romero, J. Opt. Soc. Am. A **11**, 107–117 (1994).
[16] W. Lu *et al.*, Phys. Rev. Spec. Top. - Accel. and Beams **10**, 061301 (2007).
[17] D. H. Froula et al., Phys. Rev. Lett. **103**, 215006 (2009).
[18] A. Pukhov, J. Plasma Phys. **61**, 425 (1999).
[19] J. Viera *et al.*, Plasma Phys. Control. Fusion **54**, 055010 (2012); G. Genoud *et al.*, Phys. Plasmas **20**, 064501 (2013).
[20] S. A. Yi, V. Khudik, S. Y. Kalmykov, G. Shvets, Plasma Physics and Controlled Fusion **53**, 014012 (2011).
[21] K. Y. Kim *et al.*, Appl. Phys. Lett. **81**, 4124–4126 (2002); J. K. Wahlstrand *et al.*, Phys. Rev. Lett. **107**, 103901 (2011).